

The Impulse Response of a High-Speed Jet Forced with Localized Arc Filament Plasma Actuators

Aniruddha Sinha*, Hind Alkandry†, Martin Kearney-Fischer‡ and Mo Samimy§

Gas Dynamics and Turbulence Laboratory, Aeronautical and Astronautical Research Laboratories

The Ohio State University, Columbus, OH, 43235

We present an experimental analysis of the impulse and harmonic responses of high-speed and high Reynolds number jets to arc filament plasma actuation as revealed in the phase-averaged near-field pressure. Scaling laws derived by operating the round jets at four subsonic Mach numbers and two nozzle exit diameters are used to separate the hydrodynamic component of the wave response from the actuator noise. The plasma actuator applies repetitive impulses at the nozzle lip, and the impulse response is approximated by employing forcing Strouhal numbers less than 0.1. The resulting phase-averaged signature displays a compact wave with a positive oscillation preceding a negative one. This is indicative of a large scale vortical structure that develops from each impulsively seeded perturbation. As the forcing frequency increases, the compact waves are seen to fuse together at first. With further increases in frequency, the seeded structures appear to be competing for the energy that is to be extracted from the sheared mean turbulent flow. Superposition of the periodically phase-shifted impulse response replicates the harmonic response reasonably well, demonstrating the quasi-linearity of structure interaction with low forcing frequencies. The present analysis thus provides another perspective on the jet column mode instability which is usually invoked to explain the existence of an optimum forcing frequency for mixing enhancement.

Selected Nomenclature

D	Nozzle exit diameter, m
M_j	Nozzle exit Mach number
Re_D	Reynolds number based on D and nozzle exit conditions
St_D	Spectral Strouhal number based on D (fD/U_j)
St_{DF}	Forcing Strouhal number based on D ($f_F D/U_j$)
St_D^{\max}	Strouhal number at the spectral peak
T	Phase-time measured from the starting time of an actuation pulse (s)
T_{pp}	Time from positive peak to succeeding negative peak of wave component pressure (s)
U_c	Convective velocity (m/s)
U_j	Nozzle exit velocity (m/s)
a_0	Speed of sound in ambient (m/s)
f	Spectral frequency (Hz)
f_F	Forcing frequency (Hz)
p	Pressure, normalized by $\rho_j U_j^2$
p_{MS}	Mean square pressure, normalized by $(\rho_j U_j^2)^2$
\tilde{p}	Phase-averaged or ‘wave’ pressure, normalized by $\rho_j U_j^2$
r	Radial coordinate (m)

*PhD candidate, Currently Postdoctoral Scholar at California Institute of Technology, AIAA member

†Graduate Student in Dept. of Mechanical and Aerospace Engineering, AIAA student member

‡PhD candidate, Currently Sr. Aeronautical Engineer at Lockheed Martin Aeronautics, AIAA member

§The Nordholt Professor of Engineering, Dept. of Mechanical and Aerospace Engineering, AIAA fellow, Corresponding author, samimy.1@osu.edu

x	Axial coordinate measured downstream of the nozzle exit (m)
ρ_j	Nozzle exit density (kg/m^3)
D1	Jet formed with $D = 25.4$ mm (1 inch)
D1.5	Jet formed with $D = 38.1$ mm (1.5 inches)
LAFPA	Localized arc filament plasma actuator
LSS	Large scale structure
NFP	Near-field pressure
PSD	Power spectral density

I. Introduction

Active flow control has been applied to high-speed and high Reynolds number jets with several objectives, chief among them being: (a) noise mitigation, and (b) mixing enhancement. In addition to these practical goals, the organization of the flow afforded by active flow control may also be used as a diagnostic aid to facilitate understanding of the essential physics.

Localized arc filament plasma actuators (LAFPAs) have been developed and implemented for active control of jets at the Gas Dynamics and Turbulence Laboratory (GDTL) in the Ohio State University over almost a decade.¹⁻⁴ Each LAFPA consists of a pair of electrodes placed very near the nozzle exit, connected to a high voltage source through a switching circuitry. Closing the switch causes the voltage across the electrodes to rise until the air between them undergoes breakdown, which injects a perturbation to the flow. Controlling the periodicity of switching as well as the order of switching of the LAFPAs arranged around the nozzle exit periphery allows metered injection of high-amplitude perturbations into the flow.

Characterization of LAFPAs has been performed with several measurement techniques, viz.: particle image velocimetry (PIV), schlieren imaging, flow visualization, and acoustic measurements in both the far-field and intermediate field. These methods have demonstrated that the LAFPAs have significant control authority on jets over a large range of Mach numbers and temperatures, for both the objectives stated above.^{3,5-11}

The near-field pressure (NFP, henceforth) has also been assayed, but not as exhaustively as the other investigations listed.¹² The present research is aimed at using NFP measurements to further characterize the effect of LAFPA forcing on jets. The NFP offers certain distinct advantages in this regard, consisting as it does of both hydrodynamic and acoustic fields.^{13,14} The acoustic field is the propagative part of the pressure field characterized by sonic phase speed. The hydrodynamic pressure is the reactive part characterized by subsonic phase speed; it contains the convective signature of the large-scale structures (LSS, henceforth) in the shear layer. NFP measurements must be made very close to the shear layer in order to obtain a strong signature of the LSS, since the hydrodynamic field dominates there but decays quickly with radial distance.¹³⁻¹⁶ Owing to the wavenumber-filtering effect in the pressure field, the NFP affords a natural low-pass filtering that rejects the signature of the finer scales of turbulence.¹⁷ Active control manipulates the LSS, and thus probing the NFP allows a convenient assessment of the forcing effect. Additionally, pressure, being a scalar, is easier to measure than the velocity field within the shear layer. Finally, the NFP probes do not impinge into the shear layer, thereby affording a non-intrusive measurement.¹⁶

Previous attempts at active flow control of jets have used acoustic drivers,¹⁸⁻²⁰ piezoelectric synthetic jets,²¹ and fluidic injection.²²⁻²⁵ The perturbations injected into the flow by these actuators are typically characterized by smooth waveforms with independent control of the amplitude. The distinguishing feature of the LAFPAs is the impulsive nature of the breakdown that injects the perturbation, and the lack of control over its amplitude. This allows a study of the impulse response of the jet. Apart from offering a window into the details of the control mechanisms at play, the knowledge of the impulse response is also crucial for model design aimed at feedback control (e.g. Ref. 26). It will be shown here that the impulse response is essentially the response of the jet to very low-frequency operation of the LAFPAs. The response to higher frequencies of LAFPA pulsation is deemed harmonic.

Previous investigations have revealed that forcing with LAFPAs has the effect of organizing the jet shear layer.^{3,6,7,10} This means that LSS are created in the flow with periodicity (in both time and azimuth) closely matching the excitation. Thus, it is logical to acquire the phase of LAFPA operation simultaneously with NFP measurements. Then, in subsequent post-processing, a phase-averaging of the NFP record may be performed to reveal the impulse response of the jet to LAFPA forcing in an average sense.

The working hypothesis in this research is that each impulse of the LAFPA seeds a perturbation in the

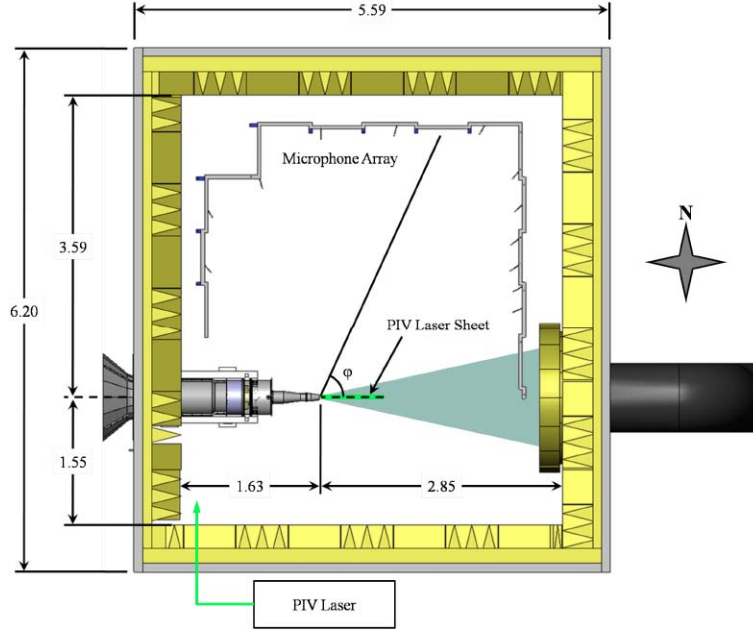


Figure 1. Schematic of the anechoic chamber and jet with measurement tools. Dimensions are in metres.

Table 1. Reynolds numbers $Re_D (\times 10^{-6})$ at the jet operating conditions.

D	M_j			
	0.80	0.85	0.90	0.95
25.4 mm (D1)	0.56	0.61	0.66	0.71
38.1 mm (D1.5)	0.84	0.91	0.98	1.06

initial shear layer that grows and rolls up into an LSS. Scaling laws derived from the phase-averaged impulse and harmonic responses under a range of operating conditions will be used to investigate this premise.

II. Experimental Setup

A. Test Facility

All the experiments are conducted in the newly upgraded anechoic chamber at GDTL within the Aeronautical and Astronautical Research Laboratories (AARL) at Ohio State University. A schematic of the chamber is shown in Figure 1. The design and validation has been documented in Ref. 27. The ambient air is compressed using three 5-stage reciprocating compressors, filtered, dried, and stored in two cylindrical 36 m³ tanks at up to 16 MPa. The stagnation pressure immediately upstream of the jet is controlled to maintain the pressure within 0.2 psi of the desired value. The air is discharged horizontally through the nozzle into the anechoic chamber, and then through an exhaust system to the outdoors (see Figure 1).

The present work employs two similar converging axisymmetric nozzles, differing only in their exit diameters D . The two exit diameters are 25.4 mm (1 inch) and 38.1 mm (1.5 inches), and the respective nozzles would be denoted as D1 and D1.5 in the rest of this article. The internal contours of the nozzles are designed using a 5th order polynomial. The nozzles are operated at four subsonic exit Mach numbers M_j , and these are indicated in Table 1. The jets were not heated, and the stagnation temperature typically stayed between 5 and 15°C. Quasi-one-dimensional isentropic compressible flow relations²⁸ are used to compute the flow variables at the jet exit from the stagnation temperature and pressure, and Sutherlands formula²⁹ is used to calculate the dynamic viscosity at the jet exit. The Reynolds number Re_D based on D and the exit

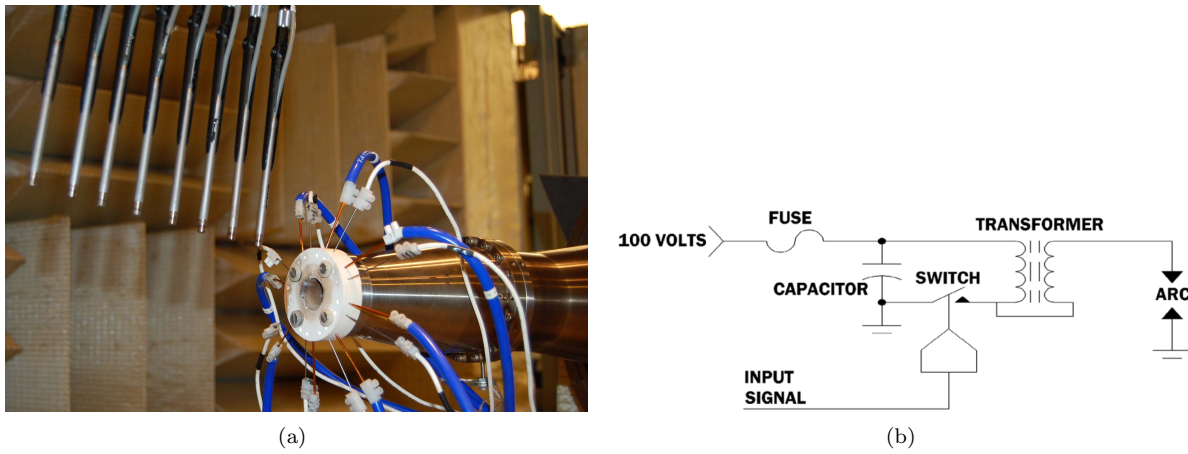


Figure 2. (a) Photograph of LAFPAs housed in ceramic nozzle extension, and linear array for measuring near-field pressure. (b) Schematic of high-voltage circuitry for one LAFPA channel.

conditions are as shown in Table 1 for the operating conditions reported herein. Previous measurements indicate that the shear layer is turbulent at the nozzle exit for all the operating conditions.⁷

B. Localized Arc Filament Plasma Actuators

As discussed in the introduction, GDTL has developed a type of flow control actuator known as localized arc filament plasma actuator (LAFPA). Each actuator consists of a pair of pin electrodes held in place using a nozzle extension (see Figure 2(a)). Eight such actuators are uniformly distributed around the nozzle perimeter, approximately 1 mm upstream of the nozzle extension exit plane. A ring groove of 0.5 mm depth and 1 mm width is used to house the electrodes and to shield the plasma. The nozzle extension is made of boron nitride and tungsten wires of 1 mm diameter are used for electrodes. The nozzle extension for D1.5 was built earlier, and the spacing between the pair of electrodes in an actuator is 3 mm, measured center-to-center at the arcing tips. The D1 nozzle extension was designed more recently, and advances in the circuitry of the LAFPA power supply allowed the tip separation to be increased to 4 mm without loss of reliability in arcing. Increasing the tip separation increases the breakdown voltage, and the amplification of the resulting perturbations delivers greater control authority. However, as a consequence of this difference between the two nozzle extensions, the resultant NFP amplitudes cannot be directly compared. The time-domain characteristics of the NFP in the two cases are still amenable to comparison.

A second-generation eight-channel high-voltage DC plasma generator, designed and built in-house at AARL, is used to drive the actuators. The circuitry for a single channel is depicted in Figure 2(b). The capacitor is charged to 100 Volts DC. At this time the switch is open so no current flows in the transformer. After the capacitor has been charged, a signal ($7 \mu\text{s}$ pulse) from the controlling computer closes the switch and keeps it closed for the duration of the pulse. There is now a complete path from the charged capacitor to the transformer. The capacitor discharges through the primary coil generating a magnetic flux field inducing a high voltage in the secondary coil. This secondary voltage increases until it is high enough to overcome the resistance of the electrode gap and a plasma generating arc is formed. This arc has a duration of about $6 \mu\text{s}$ beyond the trigger turn off while the transformer de-energizes. At the end of control pulse the switch again opens up and the capacitor recharges. This cycle can repeat to a maximum of 20,000 times per second (20 kHz) with the second-generation power supply system, the limitation being imposed at present by the cooling requirements. The cooling system is currently being upgraded to increase the frequency capability to 100 kHz.

The actuator system allows independent control of firing frequency as well as the order of firing around the periphery (azimuthal mode). The forcing frequency is varied from 250 Hz to 15 kHz in non-uniform increments in the present experiments. All actuators are fired simultaneously, thereby simulating axisymmetric forcing. Based on previous studies of the effect of varying the pulse width,³⁰ it is fixed at $7 \mu\text{s}$ in these experiments, as mentioned above. Note that the LAFPA system does not admit direct control of the amplitude of the perturbations injected.

C. Data Acquisition

1. Near-Field Pressure Measurements

The NFP is acquired using a linear array of eight microphones in a meridional plane of the jet (see Figure 2(a)). The axial separation between microphones is 25.4 mm (1.0 inch). The axial location of the entire array can be selected as desired. For the present experiments, the most upstream microphone is placed at an axial distance of $2D$, measured from the nozzle exit plane. The tips of the sensors on the linear array form a line inclined at 8.6° to the jet axis. The radial location of the most upstream microphone is $1.35D$. This configuration ensures that the sensors are approximately equidistant from the outer edge of the shear layer of the unforced $M_j = 0.9$ jet, as measured in earlier PIV assays.⁷ The conical configuration and axisymmetry of the jet allow the sole specification of the axial coordinate of a sensor to fully determine its spatial location. The 1/4 inch Bruel & Kjaer (B&K) (model 4939) microphones are paired with B&K pre-amplifiers (model 2670). The excitation signal to the microphones, as well as the amplification and filtering of the output, are performed on B&K Nexus signal conditioners (model 2690). The circuitry of the microphones was found to be robust to the electro-magnetic interference arising from the LAFPA.

The voltage signal from each microphone is band-pass filtered between 20 Hz and 100 kHz. The amplified signals are simultaneously acquired using National Instruments (NI) PXI-6133 A/D boards and LabVIEW software. The microphones are calibrated using a 114 dB, 1 kHz sine wave, and the frequency response of the microphones is flat up to 80 kHz with the microphone grid cover removed. Signals are acquired at 200 kHz with 81920 data points per block of samples. Ten such blocks of data are recorded for each experimental case resulting in 4 seconds worth of data, which is sufficient for convergence of turbulence statistics. For calculation of power spectral densities, the short-time window is set to 8192 samples, resulting in a spectral resolution of 24.4 Hz.

2. Actuation Phase

The phase-averaging of the forcing response requires precise knowledge of the actuation signal corresponding to each pressure sample. In each experimental run with forcing, a unique forcing frequency is employed and all the LAFPA are fired simultaneously. The particular character of LAFPA described above then means that the only unknown forcing information at any time is its phase. A sampling frequency of the order of MHz would have been required to determine the phase from the rectangular pulse train controlling the LAFPA operation. Instead, the pulse train controlling the first LAFPA is supplied to an Agilent 3320A 20 MHz arbitrary waveform generator, where each of the square rising edges on the rectangular pulse train triggers a rising ramp signal. This sequence of ramp signals is acquired simultaneously with the pressure signals using the NI hardware and LabVIEW program described above. The output from the waveform generator is high at 5 V by default. Each ramp rises from 0 to 5 V within 50 μ s, which is shorter than the smallest forcing time-period of interest, while being long enough to be sampled multiple times at the 200 kHz sampling rate. In post-processing of forcing cases, the ramp signal is decoded to determine the actuation phase at each pressure sample. An example of the ramp signal appears subsequently in Figure 6.

III. Unforced Jet Results

A preliminary characterization of the near-field pressure in the unforced jet situates the ensuing discussion of the impulse response. The availability of data over the range of nozzle exit velocities and the two nozzle exit diameters also affords a unique opportunity to evaluate some of the commonly used scaling laws in NFP analysis.

The established normalization for the near-field pressure fluctuation amplitude, p , at least for cold subsonic jets, is the nozzle exit dynamic head $\rho_j U_j^2$, where ρ_j and U_j are the exit density and axial velocity respectively.^{13,14} This scaling is implied for all NFP data presented, unless otherwise mentioned. The NFP spectral frequency, f , is always converted to the non-dimensional Strouhal number, $St_D = fD/U_j$. The NFP amplitude and frequency are functions of the measurement location, but these are not addressed in the above normalizations. The axial distance, x , from the nozzle exit plane and the radial distance, r , from the jet centerline are normalized by D .

The mean-square (or equivalently, variance) of the pressure fluctuations, p_{MS} , in the unforced jet are presented in Figure 3. The nozzle exit dynamic head is collapsing the data relatively well over this range

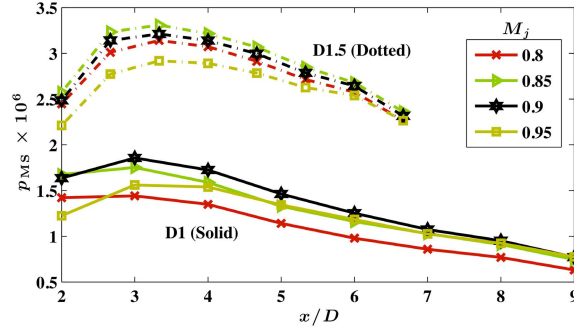


Figure 3. Mean-square of near-field pressure fluctuations in unforced jets.

Table 2. Convective velocity U_c/U_j from unforced jet correlations at $x = 4D$.

D	M_j			
	0.80	0.85	0.90	0.95
D1	0.70	0.71	0.71	0.72
D1.5	0.69	0.71	0.72	0.71

of Mach numbers. The growth and decay of the NFP amplitude with axial distance has been well documented.^{15,31,32} The NFP is primarily hydrodynamic at the array location (see following discussion). Thus, this behavior of p_{MS} in Figure 3 is indicative of the corresponding dynamics of the LSS that are evolving downstream.

The degree of collapse is better for D1.5 than for D1, the reason for which is not known. Although the r/D location of the microphone array was kept the same for the NFP measurements in D1 and D1.5, the scaled p_{MS} values do not match. Except for the most upstream observation locations, though, the trends are similar. The precise placement of the near-field sensor array relative to the nozzle exit is challenging, and the near-field decays rapidly. Apart from this possible explanation of the discrepancy from the measurement aspect, a second reason may be sought in the differences of the contraction ratios in the two nozzles. The D1 nozzle, with the more aggressive contraction, may have lower turbulence levels in the boundary layer at exit, making it inherently ‘quieter’. The significant contribution of the nozzle internal geometry to jet development and far-field acoustics has recently received renewed attention (e.g. Ref. 33). In any case, this lack of D -scaling of the spatial dependence of the p_{MS} field precludes direct comparison of the *amplitudes* recorded with the two different nozzles. Such a comparative exercise is also disallowed by the differences in the LAFPA strengths between D1 and D1.5, as mentioned in Section II.

A notion of convective velocity, U_c , of the LSS can be obtained from a space-time cross-correlation of the NFP signals measured at two axial stations.^{31,32} The convective velocity is known to scale with the centerline velocity, and thus decreases downstream of the potential core. The correlation method was used to calculate U_c/U_j at $x = 4D$, and the results are presented in Table 2. The value of U_c/U_j remains very close to 0.7 independent of the jet operating conditions tested. A value of 0.69 was also reported for a Mach 0.85 jet with $D = 50.8$ mm.³² These values are higher than the typical value of 0.6 reported for low subsonic jets,¹³ although a factor of 0.7 was reported for a Mach 0.3 jet.¹⁴ Moreover, a value of 0.58 was reported for the Mach 0.9 jet with 25.4 mm exit diameter operated at GDTL; this was computed by using cross-correlation of conditionally-averaged particle image velocimetry data in the shear layer.⁷ This diversity reflects the difficulty in defining and measuring the convective velocity in high-speed jets.

Figure 4(a) presents the power spectral density (PSD) plots for the unforced jets measured at $x = 4D$, $r = 1.65D$. A good collapse of the data is observed with the scaling using Strouhal number and the nozzle exit dynamic head, barring the discrepancy in the results between D1 and D1.5.

Ref. 13 analytically showed that the change in the slope of the NFP spectrum, noted at $St_D \approx 0.6$ in Figure 4(a), is indicative of the demarcation between the hydrodynamic and acoustic frequential components

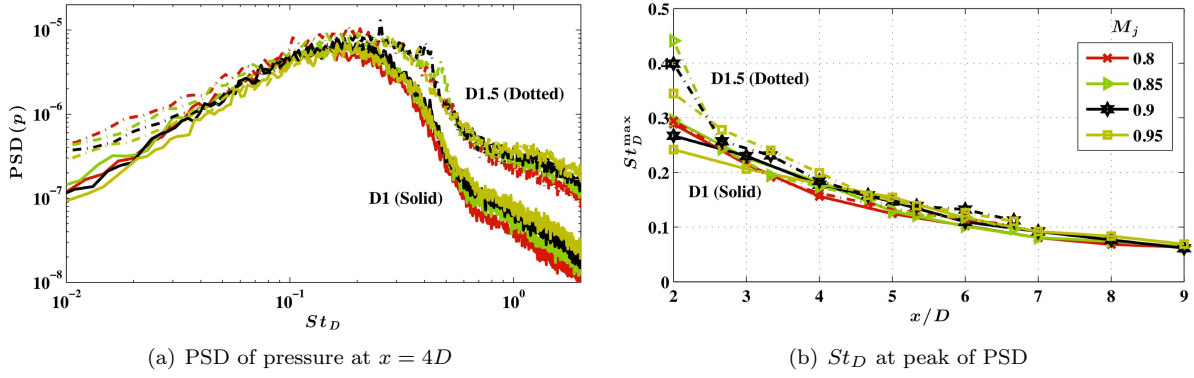


Figure 4. Spectral character of NFP in unforced jets.

of the NFP. The critical frequency was reported in terms of ky . Here, k denotes the wavenumber and y refers to the radial distance of the NFP sensor from the lip-line, which is assumed to be an approximate location of the source of the pressure fluctuations. For negligible dispersion in the irrotational near-field, $k = 2\pi f/a_0$, where f refers to spectral frequency and a_0 is the ambient speed of sound. The demarcation in the spectrum was reported as $ky \approx 2$ for low subsonic jets.^{13,14,34} For a Mach 0.85 jet the critical value was found to be $ky \approx 3.5$.^{35,36}

Figure 4(a) indicates that the demarcation is occurring at $St_D \approx 0.6$ for *all* the Mach numbers and jet diameters studied. At $x = 4D$, the radial distance $y = 1.15D$. Thus, the ky value for the change-over varies between 3.5 and 4.1 for the range of Mach numbers studied here. This agrees very closely with the results from the Mach 0.85 jet stated above. A better collapse of the critical frequency may be obtained with fy/U_c than ky . This was indeed verified for all the measurement locations and Mach numbers in both D1 and D1.5, and a very consistent value of unity was found. Moreover, for the 170 m/s exit velocity and convective Mach number of 0.3 reported in Ref. 13, the $ky = 2$ factor also converts to a value of $fy/U_c = 1$. Since the factor U_c/U_j is 0.6 in Ref. 13, scaling the critical frequency by U_j would not have yielded this match. By definition, U_c/f is the axial wavelength of a structure of frequency f . Thus, the above scaling of the critical frequency is indicating that the character of the NFP associated with a structure is changing to acoustical at a radial distance approximately equal to the corresponding axial wavelength of the large-scale structures. This is an intriguing observation.

In Figure 4(a), the spectral change to acoustic character is occurring between 1 and 2 orders-of-magnitudes below the peak. Thus, the NFP is predominantly hydrodynamic at the location of the sensor array. This means that the spectral peak frequency reflects the temporal character of the most dominant large-scale structures. Figure 4(b) presents the Strouhal number at the spectral peak, St_D^{\max} , over the range of measurement locations and jet operating conditions. Prior to the peak determination, the spectral curves are smoothed by a moving average filter whose window size increases with frequency to yield an undistorted curve in the logarithmic scale.

The decrease in St_D^{\max} with axial distance from the exit has been discussed in the literature,^{13,31,32} and this has been linked to the growth of the shear layer. In particular, Ref. 13 noted that multiplying the spectral frequency by $(x - x_0)$ can collapse the spectra between $x \approx 3D$ and the end of the potential core due to the self-similarity in this range. Here, x_0 is a fitting constant. The St_D^{\max} values in Figure 4(b) exhibit relatively greater scatter at the first sensor location, but are indeed very well collapsed downstream of $x \approx 3D$. A least-squares fit for the St_D^{\max} data for $x \geq 3D$ yielded the following relation

$$St_D^{\max}(x/D - 0.91) = 0.54, \quad (1)$$

with coefficient of determination $R^2 = 0.92$. The axial extent of the sensor array is insufficient to discriminate the above fit beyond the end of the potential core.

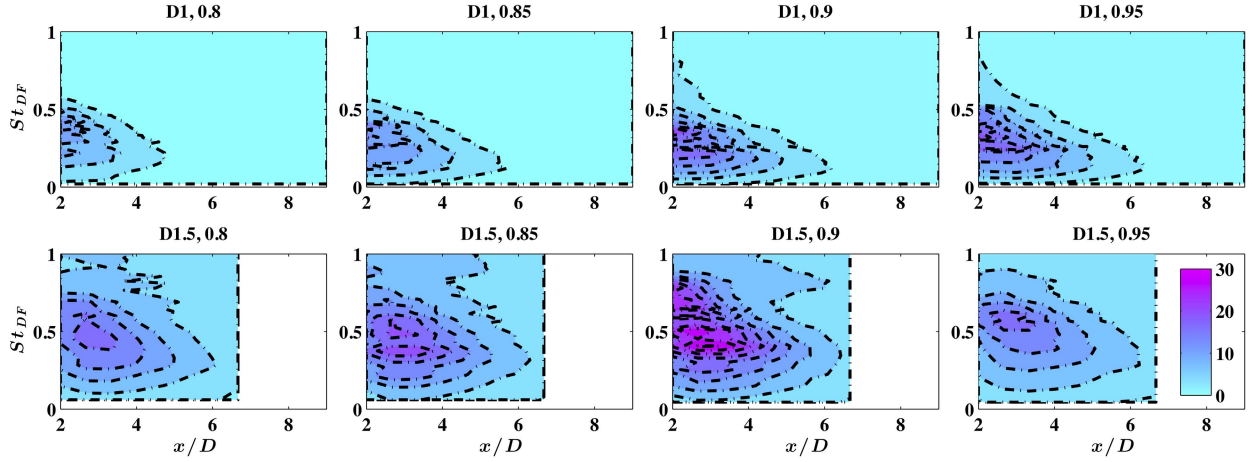


Figure 5. Mean-square of near-field pressure fluctuations ($\times 10^6$) with forcing. The sub-figure titles indicate the nozzle case and M_j .

IV. Forced jet results

The three-dimensional parameter space of subsonic Mach number ($M_j < 1$), nozzle exit diameter (D1 and D1.5), and forcing frequency, f_F , is swept to determine the forcing response of the jet using the NFP measurements. The linear array of NFP probes is held fixed at the location mentioned earlier. The forcing frequency is normalized to the forcing Strouhal number $St_{DF} = f_F D/U_j$ as usual, and one of the objectives here is to evaluate this scaling law.

A. Time-averaged response

The simplest metric of the time-averaged response of the NFP is p_{MS} , and this is documented for the entire parameter space in Figure 5. The following observations are made:

- The amplitude-effect of forcing is frequency-dependent. At any spatial location, increasing the St_{DF} rapidly increases the p_{MS} followed by a gradual decrease.
- Although no trend can be observed in the amplitudes with M_j , there is quite a lot of variability, much more than the observed variations in the unforced jet in Figure 3.
- The peak St_{DF} decreases with downstream distance of the measurement location, much like the decrease in St_D^{max} in the unforced jet (see Figure 4(b)).
- The peak St_{DF} appears to be independent of M_j , and similar behavior was also noted for St_D^{max} .
- The general shape of the contours described above is similar for all the jet operating conditions displayed. However, there are significant differences too.
 - The maximum amplitude effect in the case of D1 is measured at the most upstream sensor. On the contrary, for the D1.5 case, the peak is observed at $x = 3D$. A similar discrepancy can also be noted in the unforced jet results in Figure 3.
 - In general, the p_{MS} for D1.5 are higher than those for D1, and this trend also follows the corresponding behavior observed in the unforced jet. It must be recalled though, that the nozzle extensions in D1 and D1.5 have different tip-separation of the LAFPA (4mm vs. 3mm). The increased tip-separation is expected to produce greater perturbation. The comparatively lower amplitudes observed in D1, posing as it does the reverse trend, cannot be explained by the LAFPA strength.
 - The peak St_{DF} is consistently higher for D1.5 compared to D1. This is not reflected in the St_D^{max} plots presented in Figure 4(b).

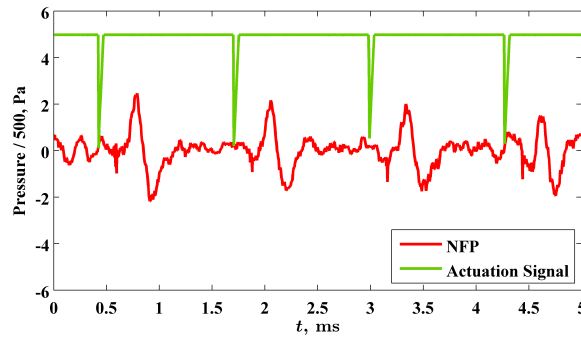


Figure 6. Response of NFP at $x = 2D$ for Mach 0.9 D1 jet forced at 770 Hz. The falling edges of the ramp signal indicates the instants at which the LAFPA are switched on.

The collapse of the results (with the caveats mentioned) with the proposed scaling provides evidence that the perturbations imparted by forcing are extracting energy from the flow and generating LSS.

B. Wave response

The main interest in the present analysis is the new information that the simultaneous acquisition of the actuation phase provides. Figure 6 depicts the relationship between the NFP and the actuation. It is clear that each LAFPA firing is triggering a pressure pulse that rises well above the baseline fluctuations.

The triple decomposition³⁷ is a convenient tool to analyze periodically forced flows. For the NFP, the mean value is the uniform ambient pressure, and thus the decomposition is simplified. The instantaneous fluctuating pressure is then written as

$$p = \tilde{p} + p', \quad (2)$$

where \tilde{p} is the ‘wave’ component of the pressure, and p' is the residual ‘turbular’ part. For a known forcing frequency f_F , the wave component is computed by the following phase averaging technique

$$\tilde{p}(T; f_F) := \lim_{N \rightarrow \infty} \frac{1}{N} \sum_{n=0}^{N-1} p(T + n/f_F). \quad (3)$$

Here, T refers to the phase-time measured from the starting time of an actuation pulse. To avoid phase ambiguity, T is not bounded within 0 and $1/f_F$ in the above definition, so that \tilde{p} itself is periodic.

The wave component of the NFP response in forced jets is computed in the following steps:

1. The expected time-of-arrival is computed for each sensor location assuming that the seeded perturbation travels to a downstream sensor approximately at the convective velocity, U_c . Note that this time delay estimation is made independent of St_{DF} , but it depends on the jet operating conditions through the changing U_c .
2. For each sensor, a time window is defined with center at the expected time-of-arrival and width equal to 15 flow time units, (U_j/D) . This is assumed to be sufficiently long to fully capture the wave component of the response even if $St_{DF} < 1/15$. The subsequent results bear out this assumption.
3. The temporal beginning of each forcing pulse is determined from the recorded actuation control signal. Recall that all LAFPA are firing simultaneously in the present experiments.
4. For each pulse, the recorded pressure signal is windowed such that the zero-time of the window coincides with the beginning of the pulse.
5. The average of all such windowed signals yields the wave response of NFP at a particular sensor.

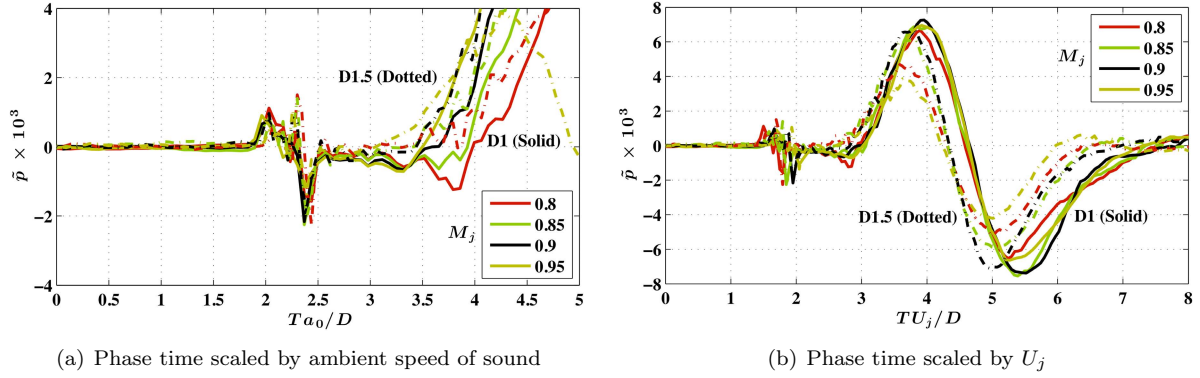


Figure 7. Impulse response of NFP at $x = 2D$ with two different phase-time scalings to highlight the (a) acoustic, and (b) hydrodynamic components. The actual forcing frequency was approximately 250 Hz.

1. Impulse Response

Figure 7 shows the wave component of NFP at $x = 2D$ for forcing at $f_F \approx 250$ Hz, which was the lowest used in these experiments. Exciting the jet at such a low frequency is equivalent to exciting it impulsively since all the relevant timescales of the jet are at least an order-of-magnitude smaller than the forcing period. The benefit of periodic forcing is the opportunity for phase-averaging afforded on data from a relatively short experimentation time. Each actuation pulse is seen to generate two well-defined compact waves, both with a positive excursion preceding a negative one.

The earlier but smaller wave is the actuator ‘self-noise’ traveling directly to the sensor without being modulated by the flow. This is revealed by the collapse of these signatures irrespective of M_j and D once the phase-time is normalized to Ta_0/D in Figure 7(a). The distance from the nozzle exit to the sensor is $2.17D$, which agrees with the observed time of arrival. Phase-locked schlieren imaging has demonstrated that each actuator pulse generates a compression wave³⁰ that is discernible near the nozzle, and this is being captured by the sensors in the near-field. The actuator self-noise dissipates quickly, becoming indistinct after the phase-averaging process at the downstream sensors. The precise shape of the signature cannot be resolved within the bandwidth of the microphones used, but a negative excursion is seen to trail the compressive wave front resulting in zero-net value.

The second compact wave generated by each actuation is much stronger, and has very different characteristics compared to the first wave, as listed below:

- This is a hydrodynamic response, as evidenced by the collapse of the time-of-arrival observed over the range of operating conditions when the phase-time is normalized by the flow time scale as TU_j/D in Figure 7(b).
- The typical size of large-scale structures at any axial station scales with the width of the shear layer, which in turn scales with x . Their convective speed, U_c , scales with U_j as shown before. Thus, the temporal persistence of a typical LSS at any station x/D scales with D/U_j . The temporal extent, T_{pp} , of the wave response recorded at a sensor in Figure 7(b) may be defined as the time from the positive to the negative peak. Its scaling with D/U_j then supports the conclusion that each LAFPA pulse generates a large-scale structure.
- At a given measurement station, the amplitudes scale with dynamic head, indicating that the response is deriving its energy from the jet flow and not from the perturbation itself.
- The negative excursion is the low pressure associated with the vortical core of the large scale structure seeded by the LAFPA perturbation. The positive peak is the compressive front that leads the LSS.
- Although the \tilde{p} signatures collapse very well for all the M_j for a given D , the collapse across the D1 and D1.5 is not as good. The lack of exact collapse can also be seen in the actuator self-noise signatures. This is probably caused by a slight error in placement of the linear sensor array in the two experiments. This issue will be revisited subsequently.

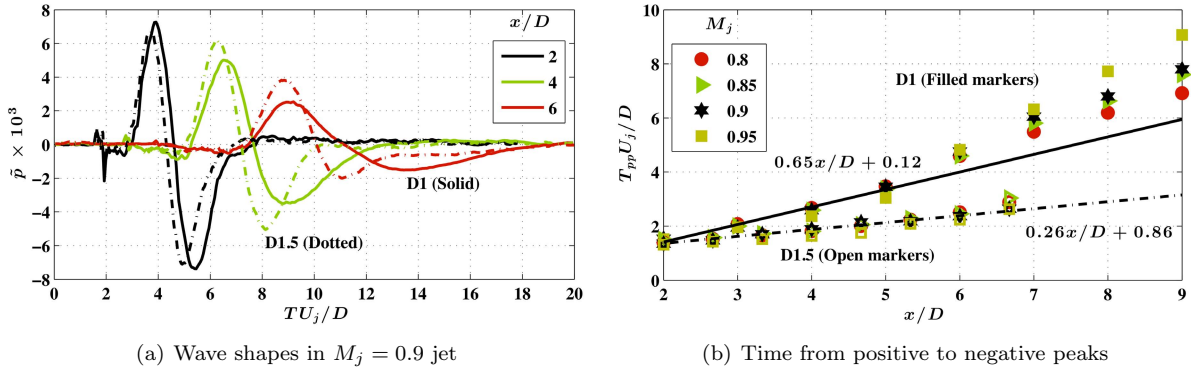


Figure 8. Axial evolution of impulse response of NFP. Filled and open markers respectively signify D1 and D1.5 data in (b).

- The minor amplitude discrepancies across different operating conditions can be expected from the corresponding discrepancies noted in the unforced jet (Figure 3) and the forced jet (Figure 5).
- There is no observed pattern to the slight variations with M_j .

Figure 8(a) investigates the axial evolution of the impulse response. As expected from the above description of large-scale structures seeded by the impulse, the convective arrival of the impulse response occurs at later times for downstream sensors. The amplitude of the response also decreases with downstream distance, as expected from the unfiltered forcing response (see Figure 5). There are noticeable differences in the characteristics between the D1 and D1.5 jets, and the investigation of this is facilitated by Figure 8(b). This focuses attention on the axial evolution of the persistence (or compactness) parameter, T_{pp} , for the range of operating conditions.

The earlier discussion has linked T_{pp} to the typical local size of the seeded LSS. The width of the shear layer scales almost linearly with x up to the end of the potential core.³⁸ Figure 8(b) also demonstrates that T_{pp} of the impulse response increases linearly up to $x \approx 6D$. This constitutes further evidence that the perturbation seeded by the impulse develops into a large-scale structure that grows with the growing shear layer. The collapse of the normalized T_{pp} values for different M_j 's also supports this view. Beyond $x \approx 6D$, the T_{pp} values depart from the initial linear behavior. This may be linked to the merger of the annular shear layer at the end of the potential core which causes distinct changes in the dynamics. For one thing, the centerline velocity starts to decrease beyond this point, which invalidates the scaling of T_{pp} with the constant U_j .

The above rationalization is hindered by the divergence of the T_{pp} values between the D1 and D1.5 jets in Figure 8(b). Although the values are very similar at $x = 2D$ (also noticeable in Figure 7(b)), they differ by a factor of two near the end of the potential core at $x = 6D$. This difference in behavior is also visible in Figure 8(a). Figure 4 has indicated that the time period ($1/St_D^{\max}$) corresponding to the spectral peak in unforced jets increases linearly with axial distance downstream. Moreover, the results for all the operating conditions were well collapsed with the standard normalizations. Although not directly comparable, the peak spectral periodicity in unforced jets and the T_{pp} in the wave component of the impulse response both reflect on the typical size of the large-scale structures in the respective cases. The collapse observed in Figure 4 vis-a-vis the divergence of the response seen in Figure 8(b) means that the impulse response cannot be directly linked to the behavior of the unforced jet.

Compared to the D1.5 nozzle, the D1 nozzle has 1.5 times greater density of LAFPA's around the periphery, and the individual LAFPA's are also expected to create stronger perturbations owing to the greater electrode tip separation. Thus, a possible explanation for the aforementioned divergence of the T_{pp} values is that the increased relative azimuthal extent of the seeded LSS in D1 is leading to their greater coalescence. Through self-inductance, this is expected to increase their size. This argument must be tempered by the stronger *amplitude* response observed with the D1.5 nozzle in Figure 5. Full-field data (flow visualization or PIV) for the D1.5 nozzle, which has not been acquired as yet, may assist in resolving this issue.

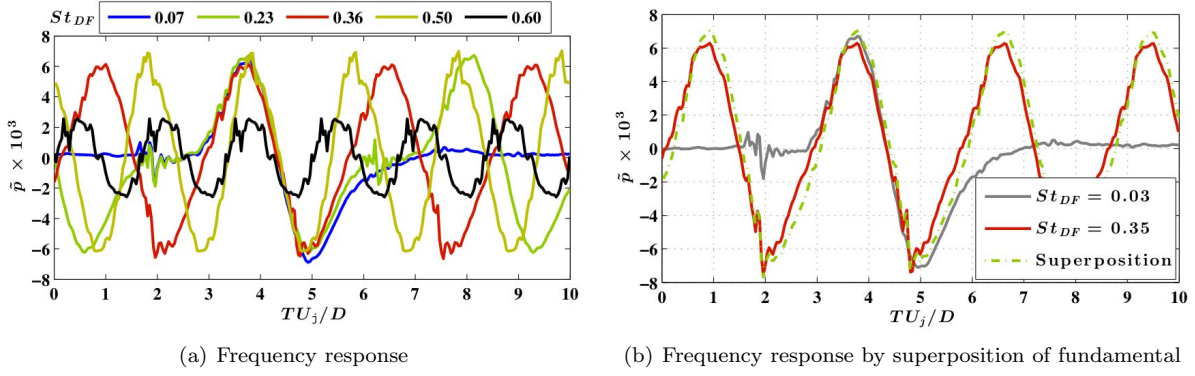


Figure 9. Wave component of NFP response of $M_j = 0.9$, D1.5 jet at $x = 2D$.

2. Harmonic Response

The foregoing phase-averaging analysis has shown that the impulse response of the jet is indicative of LSS generation. The harmonic response is now studied by employing a range of forcing frequencies covering the characteristic frequencies of the jet. Figure 9(a) depicts the wave response of the NFP in the Mach 0.9 D1.5 jet at $x = 2D$ for some salient St_{DF} 's. The $St_{DF} = 0.07$ corresponds to 520 Hz at this operating condition, and the resulting \tilde{p} is indistinguishable from the 250 Hz case presented in Figure 7(b). The fundamental response is seen to remain unchanged even at $St_{DF} = 0.23$. The periodicity only results in more pulses being captured within the averaging window. However, the actuator self-noise of the succeeding pulse is starting to encroach on the hydrodynamic fluctuation. Increasing St_{DF} to 0.36 results in an almost sinusoidal response, but the fundamental pulse shape still remains unchanged. The pulse fall-offs have sharpened at the higher St_{DF} of 0.50, although the peak-to-peak time, T_{pp} , as well as the amplitude, have not been significantly affected. Focusing on $TU_j/D \approx 2$ clarifies that the succeeding self-noise is now at the peak compression instant. By $St_{DF} = 0.60$, distinct reductions in both T_{pp} and the amplitude are observed.

Figure 9(b) investigates the linearity of the response using the following superposition operation:

1. Assume that the wave component of response for $St_{DF} = 0.03$ is the fundamental response, and denote the corresponding forcing frequency as $f_{F,0}$. Define the fundamental response in the following manner:

$$\tilde{p}_0(T) := \begin{cases} \tilde{p}(T; f_{F,0}), & \text{if } T' \leq T \leq T' + 1/f_{F,0}, \\ 0, & \text{otherwise.} \end{cases} \quad (4)$$

In the above definition, T' is arbitrary. This is the true impulse response for $f_{F,0} \rightarrow 0$.

2. For a given forcing frequency $f_F > f_{F,0}$, shift the fundamental response by $1/f_F$ and add the result to the original.
3. Repeat the above step with enough positive and negative integer multiples of $1/f_F$ so that the original phase-averaging window is fully covered.

Mathematically, the approximate wave component of response at f_F through superposition is

$$\tilde{p}(T; f_F) \approx \sum_{n=-\infty}^{\infty} \tilde{p}_0(T + n/f_F). \quad (5)$$

Figure 9(b) demonstrates that the result of the above superposition closely resembles the actual wave component of response at $St_{DF} = 0.35$. This indicates that the seeded LSS in the flow are interacting quasi-linearly with the succeeding LSS in the wave train at low St_{DF} 's. This superposition effect was replicated for all the forcing cases shown in Figure 9(a).

The next step is the quantification of the variation of the temporal persistence parameter, T_{pp} , of the wave response with St_{DF} . The \tilde{p} response curves are not very smooth owing to the superposition of the actuator

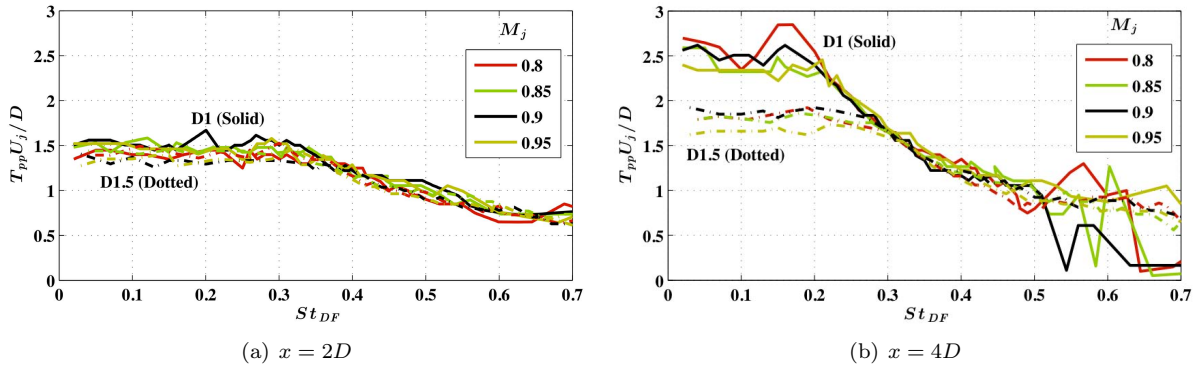


Figure 10. Time between the positive and negative peaks of the wave component of NFP response.

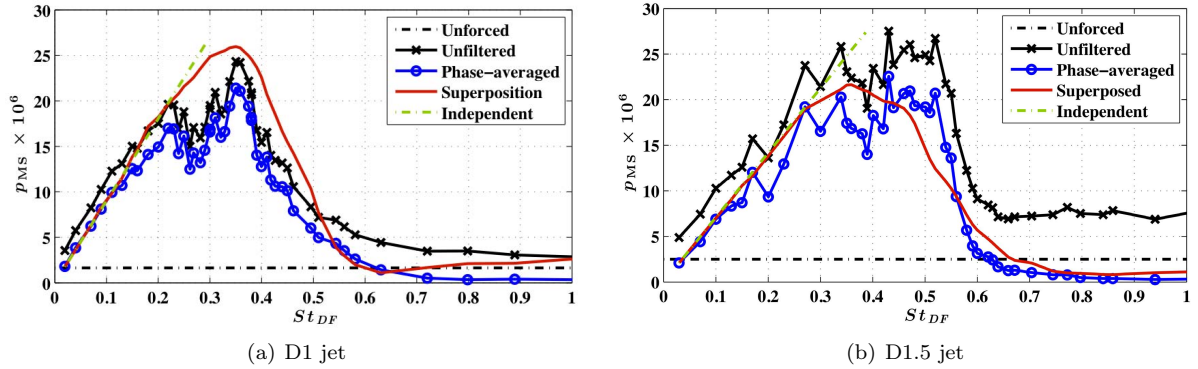


Figure 11. Comparison of mean-square pressure at $x = 2D$ in $M_j = 0.9$ jet obtained by various methods.

self-noise. Wavelet filtering is performed to smooth the curves while maintaining its compact shape.^{39,40} The 4th order Paul wavelet was chosen as the mother since its imaginary part resembles the impulse response, and wavelets with amplitude less than 25% of the maximum amplitude were rejected prior to the reconstruction. The results presented here are quite insensitive to the precise threshold, since a first-order parameter is being extracted. This filtering removed the jitters in the \tilde{p} curves while preserving the overall shape.

Values of T_{pp} determined from the wavelet-filtered harmonic responses are plotted in Figure 10(a) for the sensor at $x = 2D$. The initial flatness of the curves reflects the invariant nature of the fundamental response at these low St_{DF} 's. Moreover, as expected from Figure 7(b), the values of $T_{pp}U_j/D$ are very close over the tested range of M_j 's and D 's. Beyond a certain shoulder in the curves, there is a gradual fall-off. In a re-plotting of these curves with $2(T_{pp}U_j/D)St_{DF}$ on the ordinate (not shown here), these regions of the curves were found to be quite flat at unity. Thus, the response is essentially sinusoidal over this range of St_{DF} 's, with $T_{pp} \approx 0.5/f_F$. Beyond this range, the wave component of response becomes too uncertain to reliably determine T_{pp} .

Figure 10(b) demonstrates that the T_{pp} curves for the $x = 4D$ station have a similar behavior, except in the two aspects that were observed in Figure 8(b). Firstly, the constant T_{pp} value at the lowest St_{DF} 's is increased. The decay portions of the curves are universal as explained for Figure 10(a) above. Thus, the increase in the initial T_{pp} brings the shoulders of the curves to lower St_{DF} 's. The other aspect is the distinct divergence of the scaled initial T_{pp} 's between D1 and D1.5.

The amplitude response of the forced jet, is now revisited with the perspective gained above. Figure 11 shows the mean-square of the unfiltered pressure in the D1 and D1.5 $M_j = 0.9$ jets at $x = 2D$. These were already presented in Figure 5, so that their mutual differences will not be revisited. The mean-square NFP in the unforced jet is shown too. The mean-square is also calculated from the wave component of pressure signals, taking care to truncate the calculation to one forcing period exactly. This amounts to a narrow-band filtering of the pressure signal to extract just the forcing tone. For $St_{DF} \lesssim 0.2$, the difference between

the unfiltered p_{MS} and the phase-averaged p_{MS} in any forcing case is almost equal to the p_{MS} measured in the unforced jet. This implies that there is very little broadband spectral change, and the forcing effect is concentrated at the forcing frequency. Another way of saying this is that the response is almost linear for these low frequencies. The discrepancy is more significant at the higher frequencies, implicating higher broadband and/or harmonic content of forcing response.

In the discussion regarding Figure 9(b), it was established that the periodic linear superposition of the wave component of response at a low frequency yields a good approximation of a higher frequency signature. Pursuing this idea, the superposition was performed over the range of St_{DF} 's, and the mean-square computed from these is overlaid in Figure 11. As expected, the match with the wave component of response is very good at low-frequencies, furthering the hypothesis of linearity. At frequencies near the peak response and beyond, the discrepancy is more pronounced.

The constancy of the peak-to-peak time, T_{pp} , at the lower frequencies in Figure 10 was understood to signify the lack of interaction between the periodically seeded structures. This conjecture can be further evaluated in the following manner. The \tilde{p} for the lowest frequency has compact support within one forcing period. Then, assuming independent addition of successive structures all with the same compact signature, the mean-square pressure should be directly proportional to the forcing frequency. This trend is indicated in Figure 11, and it is indeed seen to model the NFP response well up to $St_{DF} \approx 0.15$.

Structure interaction begins beyond this forcing frequency, so that independent addition is an incorrect model. Figures 9(a) and 10 reveal that the interaction does not modify T_{pp} or the peak amplitudes initially. Instead, the relaxation of the pressure field is hastened primarily. Consequently, the mean-square pressure keeps on increasing with increasing St_{DF} . However, this monotonic trend is arrested once T_{pp} starts to decrease, the shoulder St_{DF} being about 0.25 (see Figure 10). Figure 9(a) shows that the slope of the fall from the positive peak to the negative one remains unchanged to much higher frequencies. Thus, the decrease in T_{pp} is indicative of a reduction in the amplitude of the peaks of the wave component of signature. An intuitive understanding is that the neighboring structures inhibit each other's growth.

Many earlier experiments have observed the existence of an optimum frequency for mixing enhancement.^{3,6,10,41} This has been explained as a resonance with the jet column mode, which, in turn, is taken to imply the natural frequency of the undulation of the jet column or potential core. In this research, the observations in the phase-averaged near-field pressure response afford another perspective on this behavior based on interactions of the periodically seeded structures. It must be noted though that Ref. 42 has previously proposed an explanation of the jet column mode in terms of the inflectional instability of the initial shear layer at the nozzle exit, and the present findings support that view.

V. Discussion and Conclusion

The near-field pressure has been probed to investigate the response of subsonic jets to forcing with localized arc filament plasma actuators (LAFPA). These actuators have demonstrated superior control authority on high-speed turbulent jets over a wide range of practical operating conditions. Four subsonic Mach numbers ($M_j = 0.80$ to 0.95) and two different nozzle exit diameters ($D = 25.4$ mm and 38.1 mm) are investigated to discern scaling laws for the response of the jet. The arc breakdown imparts an impulsive perturbation to the flow each time an actuator is switched on. Eight LAFPA uniformly arrayed around the periphery of the nozzle exit are operated in phase to simulate axisymmetric forcing. Phase-averaging of the pressure signal with respect to the actuator signal has been leveraged to separate the relevant features of the response from the background turbulence. Although the LAFPA switching is periodic, the forcing regime is conveniently categorized as either impulse or harmonic depending on the frequency.

At forcing Strouhal numbers less than 0.1, the phase-averaged pressure signature displays a compact sinusoidal wave with one positive excursion preceding one negative excursion. Scaling of the parameters of this wave with the nozzle exit velocity indicates that this response is hydrodynamic. There is a second compact wave in the phase-averaged pressure signature – but this is much smaller in amplitude, decreases rapidly with downstream distance from the nozzle, and is determined to be the actuator noise traveling with the ambient speed of sound. Since the time scale of the hydrodynamic response is much shorter than the forcing period employed to generate it, this is deemed the impulse response. The conclusion is that each actuator impulse is creating a flow perturbation which extracts energy from the flow to develop into a large scale structure. The negative peak in the near-field pressure is associated with the core of the seeded structure and the positive excursion is the compressive front leading it. Owing to the impulsive nature of the

actuator, this appears to be a very robust and reliable method of generating a single structure with precise timing in the highly turbulent flow.

The time scale of the compact impulse response observed at an axial station increases with its downstream distance from the nozzle exit. This is indicative of a growing structure. At a given station, the character of the impulse response is unchanged for all forcing frequencies as long as the corresponding forcing period is longer than local time of persistence. In other words, for forcing frequencies below a certain threshold each seeded structure evolves and convects without interacting with its predecessor or successor. The threshold frequency is inversely proportional to the downstream distance of the measurement station. Owing to the independent evolution of the structures in this forcing regime, the mean-square pressure measured is directly proportional to the forcing frequency. Beyond this frequency threshold, the phase-averaged pressure signature must be termed the harmonic response as the structures interact with each other, the effect being discernible in the modification of the response wave shape.

The structure interaction initially manifests in a sinusoidal phase-averaged pressure signature where the relaxation associated with a structure passage is immediately followed by the compression leading the succeeding structure. As forcing frequency increases, the pressure fall from the positive peak to the negative peak remains unchanged, their amplitudes also remain unaffected, but the succeeding pressure rise is sharper. Thus, the mean-square pressure, although still increasing, starts to deviate from the linear increase with forcing frequency. However, the structure interaction appears to be quasi-linear – the wave shape can be reconstructed reasonably accurately by linear superposition of the fundamental impulse response with the forcing periodicity. This is a novel result.

The trend of increasing mean-square pressure response with forcing Strouhal number is reversed beyond a certain value that depends on the observer location. For example, the peak response is observed with approximate Strouhal numbers of 0.35 and 0.2 respectively at $2D$ and $4D$ downstream of the nozzle exit. Looking to the phase-averaged pressure response, the change is discernible in the reduced amplitudes of the positive and negative peaks. The resulting wave shape is also predicted well by the linear superposition. Intuitively, a structure's natural development through extraction of energy from the sheared mean flow is being arrested by the competing structure that is succeeding it closely. Although the actual mean-square pressure vs. forcing Strouhal number curve is not exactly replicated by the one reconstructed from linear superposition of the fundamental response, the discrepancies are not large. This implies that the nonlinear effects of forcing, discernible as harmonics of the forcing tone and broadband increase in the pressure spectrum,¹² are relatively minor. The foregoing discussion offers a new perspective on the jet column mode instability that is invoked to explain the peak in the jet forcing response at an approximate Strouhal number of 0.3.

Our previous investigations have established that at high enough forcing Strouhal numbers, the mean-square near-field pressure decreases below that observed in the unforced jet, paralleling the significant mitigation of the far-field noise. This benefit of LAFPA application is of urgent practical interest to the aviation community. However, the phase-averaging technique pursued here is inappropriate for studying this important forcing regime. Beyond a certain forcing Strouhal number (~ 0.5 at $4D$ downstream), the wave response becomes statistically uncertain.

The pressure response collapsed well with appropriate scaling for the investigated Mach numbers. However, the collapse for the two nozzle exit diameters was not satisfactory. In fact, the two jets displayed significantly different linear axial growth rates of the persistence time of the impulse wave response. On the other hand, the inverse-linear axial decrease of the spectral peak frequency for the *unforced* jets were well collapsed for all operating conditions. In the absence of flow field data for the larger nozzle, no satisfactory explanation can be proposed for this disparity of behavior. At the most upstream measurement location ($2D$ from the nozzle exit), the persistence time of the compact impulse wave response is not too dissimilar from the spectral peak periodicity in the corresponding unforced cases. However, owing to the disparity mentioned above, this simple connection between the unforced and forced jet behaviors is not maintained further downstream.

In summary, the impulse and harmonic response of turbulent jets has been studied using LAFPAs. Important insight is gleaned regarding the quasi-linearity of the near-field pressure response as well as interactions of the seeded structures. In particular, the peak response characterizing the jet column mode is explained using structure interaction. There are intriguing possibilities regarding the connection of the natural jet behavior and the response to the impulsive forcing with the LAFPAs. However, more flow field investigation is needed to resolve the differences in the behavior of jets formed by two nozzles with different

exit diameters.

Acknowledgements

The support of this research by the Air Force Office of Scientific Research with Dr. John Schmisser is greatly appreciated.

References

- ¹Samimy, M., Adamovich, I., Webb, B., Kastner, J., Hileman, J., Keshav, S., and Palm, P., "Development and characterization of plasma actuators for high-speed jet control," *Experiments in Fluids*, Vol. 37, No. 4, 2004, pp. 577–588.
- ²Utkin, Y. G., Keshav, S., Kim, J.-H., Kastner, J., Adamovich, I. V., and Samimy, M., "Development and use of localized arc filament plasma actuators for high-speed flow control," *Journal of Physics D: Applied Physics*, Vol. 40, No. 3, 2007, pp. 685–694.
- ³Samimy, M., Kim, J.-H., Kastner, J., Adamovich, I., and Utkin, Y., "Active control of high-speed and high-Reynolds-number jets using plasma actuators," *Journal of Fluid Mechanics*, Vol. 578, 2007, pp. 305–330.
- ⁴Kim, J.-H., Nishihara, M., Adamovich, I., Samimy, M., Gorbato, S. V., and Pliavaka, F. V., "Development of localized arc filament RF plasma actuators for high-speed and high Reynolds number flow control," *Experiments in Fluids*, Vol. 49, 2010, pp. 497–511.
- ⁵Samimy, M., Kim, J.-H., Kastner, J., Adamovich, I., and Utkin, Y., "Active control of a Mach 0.9 jet for noise mitigation using plasma actuators," *AIAA Journal*, Vol. 45, No. 4, 2007, pp. 890–901.
- ⁶Samimy, M., Kim, J.-H., Kearney-Fischer, M., and Sinha, A., "Acoustic and flow fields of an excited high Reynolds number axisymmetric supersonic jet," *Journal of Fluid Mechanics*, Vol. 656, 2010, pp. 507–529.
- ⁷Kearney-Fischer, M., Kim, J.-H., and Samimy, M., "Control of a High Reynolds Number Mach 0.9 Heated Jet Using Plasma Actuators," *Physics of Fluids*, Vol. 21, No. 9, 2009, pp. 095101.
- ⁸Kearney-Fischer, M., Kim, J.-H., and Samimy, M., "A study of Mach wave radiation using active control," *Journal of Fluid Mechanics*, Vol. 681, 2011, pp. 261–292.
- ⁹Kearney-Fischer, M., Kim, J.-H., and Samimy, M., "Noise control of a high Reynolds number high speed heated jet using plasma actuators," *International Journal of Aeroacoustics*, Vol. 10, No. 5-6, 2011, pp. 635–658.
- ¹⁰Kim, J.-H., Kastner, J., and Samimy, M., "Active Control of a High Reynolds Number Mach 0.9 Axisymmetric Jet," *AIAA Journal*, Vol. 47, No. 1, 2009, pp. 116–128.
- ¹¹Kim, J.-H., Kearney-Fischer, M., Samimy, M., and Gogineni, S., "Far-Field Noise Control in Supersonic Jets From Conical and Contoured Nozzles," *Journal of Engineering for Gas Turbines and Power*, Vol. 133, Aug. 2011, pp. 081201.
- ¹²Sinha, A., Kim, K., Kim, J.-H., Serrani, A., and Samimy, M., "Extremizing Feedback Control of a High-Speed and High Reynolds Number Jet," *AIAA Journal*, Vol. 48, No. 2, 2010, pp. 387–399.
- ¹³Arndt, R. E. A., Long, D. F., and Glauser, M. N., "The proper orthogonal decomposition of pressure fluctuations surrounding a turbulent jet," *Journal of Fluid Mechanics*, Vol. 340, No. 1, 1997, pp. 1–33.
- ¹⁴Coiffet, F., Jordan, P., Delville, J., Gervais, Y., and Ricaud, F., "Coherent structures in subsonic jets: a quasi-irrotational source mechanism?" *International Journal of Aeroacoustics*, Vol. 5, No. 1, 2006, pp. 67–89.
- ¹⁵Suzuki, T. and Colonius, T., "Instability waves in a subsonic round jet detected using a near-field phased microphone array," *Journal of Fluid Mechanics*, Vol. 565, 2006, pp. 197–226.
- ¹⁶Tinney, C. E. and Jordan, P., "The near pressure field of co-axial subsonic jets," *Journal of Fluid Mechanics*, Vol. 611, 2008, pp. 175–204.
- ¹⁷George, W. K., Beuther, P. D., and Arndt, R. E. A., "Pressure spectra in turbulent free shear flows," *Journal of Fluid Mechanics*, Vol. 148, No. 1, 1984, pp. 155–191.
- ¹⁸Kibens, V., "Discrete Noise Spectrum Generated by an Acoustically Excited Jet," *AIAA Journal*, Vol. 18, No. 4, 1980, pp. 434–441.
- ¹⁹Moore, C. J., "The role of shear-layer instability waves in jet exhaust noise," *Journal of Fluid Mechanics*, Vol. 80, No. 2, 1977, pp. 321–367.
- ²⁰Tanna, H. K. and Ahuja, K. K., "Tone Excited Jets, Part I: Introduction," *Journal of Sound and Vibration*, Vol. 102, 1985, pp. 57–61.
- ²¹Low, K., El Hadidi, B., Andino, M. Y., Berdanier, R., and Glauser, M. N., "Investigation of Different Active Flow Control Strategies for High Speed Jets Using Synthetic Jet Actuators," *5th AIAA Flow Control Conference, AIAA Paper 2010-4267*, 2010.
- ²²Arakeri, V. H., Krothapalli, A., Siddavaram, V., Alkisar, M. B., and Lourenco, L. M., "On the use of microjets to suppress turbulence in a Mach 0.9 axisymmetric jet," *Journal of Fluid Mechanics*, Vol. 490, 2003, pp. 75–98.
- ²³Krothapalli, A., Venkatarshnan, L., Lourenco, L. M., Greska, B., and Elavarasan, R., "Turbulence and noise suppression of a high-speed jet by water injection," *Journal of Fluid Mechanics*, Vol. 491, 2003, pp. 131–159.
- ²⁴Laurendeau, E., Jordan, P., Bonnet, J.-P., Delville, J., Parnaudeau, P., and Lamballais, E., "Subsonic jet noise reduction by fluidic control: The interaction region and the global effect," *Physics of Fluids*, Vol. 20, 2008, pp. 101519.
- ²⁵Henderson, B., "Fifty years of fluidic injection for jet noise reduction," *International Journal of Aeroacoustics*, Vol. 9, No. 1-2, 2010, pp. 91–122.
- ²⁶Ma, Z., Ahuja, S., and Rowley, C. W., "Reduced-order models for control of fluids using the eigensystem realization algorithm," *Theoretical and Computational Fluid Dynamics*, Vol. 25, No. 1-4, 2011, pp. 233–247.

- ²⁷Hahn, C., *Design and Validation of the New Jet Facility and Anechoic Chamber*, Master's thesis, The Ohio State University, 2011.
- ²⁸Anderson, J. D., *Modern Compressible Flow: With Historical Perspective*, McGraw Hill, 3rd ed., 2003.
- ²⁹White, F. M., *Viscous fluid flow*, McGraw Hill, 2nd ed., 1991.
- ³⁰Hahn, C., Kearney-Fischer, M., and Samimy, M., "On factors influencing arc filament plasma actuator performance in control of high speed jets," *Experiments in Fluids*, Vol. 51, 2011, pp. 1591–1603.
- ³¹Picard, C. and Delville, J., "Pressure velocity coupling in a subsonic round jet," *International Journal of Heat and Fluid Flow*, Vol. 21, No. 3, 2000, pp. 359–364.
- ³²Ukeiley, L. S. and Ponton, M. K., "On the near field pressure of a transonic axisymmetric jet," *International Journal of Aeroacoustics*, Vol. 3, No. 1, 2004, pp. 43–65.
- ³³Zaman, K. B. M. Q., "Effect of nozzle exit condition on subsonic jet noise," *17th AIAA/CEAS Aeroacoustics Conference*, 2011.
- ³⁴Harper-Bourne, M., "On Modelling the Hydrodynamic Field of High-Speed Jets," *10th AIAA/CEAS Aeroacoustics Conference, AIAA Paper 2004-2830*, 2004.
- ³⁵Tinney, C. E., Ukeiley, L. S., and Glauser, M. N., "Low-dimensional characteristics of a transonic jet. Part 2. Estimate and far-field prediction," *Journal of Fluid Mechanics*, Vol. 615, 2008, pp. 53–92.
- ³⁶Hall, J. W., Hall, A. M., Pinier, J. T., and Glauser, M. N., "Cross-Spectral Analysis of the Pressure in a Mach 0.85 Turbulent Jet," *AIAA Journal*, Vol. 47, No. 1, 2009, pp. 54–59.
- ³⁷Hussain, A. K. M. F. and Reynolds, W. C., "The mechanics of an organized wave in turbulent shear flow," *Journal of Fluid Mechanics*, Vol. 41, No. 2, 1970, pp. 241–258.
- ³⁸Fleury, V., Bailly, C., Jondeau, E., Michard, M., and Juve, D., "SpaceTime Correlations in Two Subsonic Jets Using Dual Particle Image Velocimetry Measurements," *AIAA Journal*, Vol. 46, No. 10, 2008, pp. 2498–2509.
- ³⁹Farge, M., "Wavelet transforms and their applications to turbulence," *Annu. Rev. Fluid Mech.*, Vol. 24, 1992, pp. 395–457.
- ⁴⁰Torrence, C. and Compo, G. P., "A Practical Guide to Wavelet Analysis," *Bulletin of the American Meteorological Society*, Vol. 79, No. 1, 1998, pp. 61–78.
- ⁴¹Samimy, M., Kim, J.-H., Kearney-Fischer, M., and Sinha, A., "High-Speed and High Reynolds Number Jet Control Using Localized Arc Filament Plasma Actuators," *Journal of Propulsion and Power*, Vol. 28, No. 2, 2012, pp. 269–280.
- ⁴²Petersen, R. A. and Samet, M. M., "On the preferred mode of jet instability," *Journal of Fluid Mechanics*, Vol. 194, 1988, pp. 153–173.